# Rabi oscillations of surface plasmon polaritons in graphene-pair arrays

**Feng Wang,[1,2] Chengzhi Qin,[1] Bing Wang,[1,*] Shaolin Ke,[1] Hua Long,[1] Kai Wang,[1] and Peixiang Lu[1,3,4]**

[1]*Wuhan National Laboratory for Optoelectronics and School of Physics, Huazhong University of Science and Technology, Wuhan 430074, China*

[2]*Institute for Quantum Materials and School of Mathematics and Physics, Hubei Polytechnic University, Huangshi 435003, China*

[3]*Laboratory for Optical Information Technology, Wuhan Institute of Technology, Wuhan 430073, China*

[4]*lupeixiang@hust.edu.cn*

[*]*wangbing@hust.edu.cn*

**Abstract:** We investigate the Bloch mode conversion of surface plasmon polaritons in a periodic array of graphene pairs with each consisting of two separated parallel graphene sheets. The employment of graphene pair as a unit cell in the array yields two Bloch modes belonging to different bands. By periodically modulating the permittivity of dielectrics between graphene along the propagation direction, the interband transitions occur and the modes will alternatively couple to each other, similar to traditional Rabi oscillations in quantum systems. The indirect Rabi oscillations can also be observed through introducing transverse modulation momentum. The period of Rabi oscillations can be optimized by taking advantage of the flexible tunability of graphene. The study suggests that the structure have applications in optical switches and mode converters operating on deep-subwavelength scale.



**OCIS codes:** (240.6680) Surface plasmons; (130.2790) Guided waves; (230.4170) Multilayers.

## References and links

1. I. I. Rabi, "On the process of space quantization," Phys. Rev. **49**(4), 324–328 (1936).
2. H. G. Lee, H. Kim, and J. Ahn, "Ultrafast laser-driven Rabi oscillations of a trapped atomic vapor," Opt. Lett. **40**(4), 510–513 (2015).
3. K. Schuh, J. Seebeck, M. Lorke, and F. Jahnke, "Rabi oscillations in semiconductor quantum dots revisited: influence of LO-phonon collisions," Appl. Phys. Lett. **94**(20), 201108 (2009).
4. M. R. Matthews, B. P. Anderson, P. C. Haljan, D. S. Hall, M. J. Holland, J. E. Williams, C. E. Wieman, and E. A. Cornell, "Watching a superfluid untwist itself: recurrence of Rabi oscillations in a Bose-Einstein condensate," Phys. Rev. Lett. **83**(17), 3358–3361 (1999).
5. V. S. Shchesnovich and S. Chávez-Cerda, "Bragg-resonance-induced Rabi oscillations in photonic lattices," Opt. Lett. **32**(13), 1920–1922 (2007).
6. Y. V. Kartashov, V. A. Vysloukh, and L. Torner, "Resonant mode oscillations in modulated waveguiding structures," Phys. Rev. Lett. **99**(23), 233903 (2007).
7. K. Shandarova, C. E. Rüter, D. Kip, K. G. Makris, D. N. Christodoulides, O. Peleg, and M. Segev, "Experimental observation of Rabi oscillations in photonic lattices," Phys. Rev. Lett. **102**(12), 123905 (2009).
8. C. N. Alexeyev, T. A. Fadeyeva, B. P. Lapin, and M. A. Yavorsky, "Generation of optical vortices in layered helical waveguides," Phys. Rev. A **83**(6), 063820 (2011).
9. G. K. L. Wong, M. S. Kang, H. W. Lee, F. Biancalana, C. Conti, T. Weiss, and P. St. J. Russell, "Excitation of orbital angular momentum resonances in helically twisted photonic crystal fiber," Science **337**(6093), 446–449 (2012).
10. H. Hu, K. Wang, H. Long, W. Liu, B. Wang, and P. Lu, "Precise determination of the crystallographic orientations in single ZnS nanowires by second-harmonic generation microscopy," Nano Lett. **15**(5), 3351–3357 (2015).
11. X. Zhang, F. Ye, Y. V. Kartashov, and X. Chen, "Rabi oscillations and stimulated mode conversion on the subwavelength scale," Opt. Express **23**(5), 6731–6737 (2015).
12. F. H. L. Koppens, D. E. Chang, and F. J. García de Abajo, "Graphene plasmonics: a platform for strong light-matter interactions," Nano Lett. **11**(8), 3370–3377 (2011).

#247890 Received 14 Aug 2015; revised 9 Nov 2015; accepted 13 Nov 2015; published 20 Nov 2015

13. A. Vakil and N. Engheta, "Transformation optics using graphene," Science **332**(6035), 1291–1294 (2011).
14. A. N. Grigorenko, M. Polini, and K. S. Novoselov, "Graphene plasmonics," Nat. Photonics **6**(11), 749–758 (2012).
15. C. Qin, B. Wang, H. Long, K. Wang, and P. Lu, "Bloch mode engineering in graphene modulated periodic waveguides and cavities," J. Opt. Soc. Am. B **32**(8), 1748–1753 (2015).
16. B. Wang, X. Zhang, X. Yuan, and J. Teng, "Optical coupling of surface plasmons between graphene sheets," Appl. Phys. Lett. **100**(13), 131111 (2012).
17. A. Auditore, C. de Angelis, A. Locatelli, and A. B. Aceves, "Tuning of surface plasmon polaritons beat length in graphene directional couplers," Opt. Lett. **38**(20), 4228–4231 (2013).
18. N. M. R. Peres, "Colloquium: the transport properties of graphene: an introduction," Rev. Mod. Phys. **82**(3), 2673–2700 (2010).
19. P. Y. Chen and A. Alù, "Atomically thin surface cloak using graphene monolayers," ACS Nano **5**(7), 5855–5863 (2011).
20. C. H. Gan, "Analysis of surface plasmon excitation at terahertz frequencies with highly doped graphene sheets via attenuated total reflection," Appl. Phys. Lett. **101**(11), 111609 (2012).
21. Y. Sun, Z. Zheng, J. Cheng, J. Liu, J. Liu, and S. Li, "The un-symmetric hybridization of graphene surface plasmons incorporating graphene sheets and nano-ribbons," Appl. Phys. Lett. **103**(24), 241116 (2013).
22. A. Yariv and P. Yeh, *Photonics: Optical Electronics in Modern Communication* (Academic, 2006).
23. B. Wang, X. Zhang, F. J. García-Vidal, X. Yuan, and J. Teng, "Strong coupling of surface plasmon polaritons in monolayer graphene sheet arrays," Phys. Rev. Lett. **109**(7), 073901 (2012).
24. H. S. Eisenberg, Y. Silberberg, R. Morandotti, and J. S. Aitchison, "Diffraction management," Phys. Rev. Lett. **85**(9), 1863–1866 (2000).
25. Y. Liu, G. Bartal, D. A. Genov, and X. Zhang, "Subwavelength discrete solitons in nonlinear metamaterials," Phys. Rev. Lett. **99**(15), 153901 (2007).
26. S. A. Maier, *Plasmonics: Fundamentals and Applications* (Springer Verlag, 2007).
27. C. Qin, B. Wang, H. Huang, H. Long, K. Wang, and P. Lu, "Low-loss plasmonic supermodes in graphene multilayers," Opt. Express **22**(21), 25324–25332 (2014).
28. K. G. Makris, D. N. Christodoulides, O. Peleg, M. Segev, and D. Kip, "Optical transitions and Rabi oscillations in waveguide arrays," Opt. Express **16**(14), 10309–10314 (2008).
29. K. Okamoto, *Fundamentals and Applications of Optical Waveguides* (Academic, 2006).
30. Z. Yu and S. Fan, "Complete optical isolation created by indirect interband photonic transitions," Nat. Photonics **3**(2), 91–94 (2009).
31. A. Y. Nikitin, F. Guinea, and L. Martin-Moreno, "Resonant plasmonic effects in periodic graphene antidot arrays," Appl. Phys. Lett. **101**(15), 151119 (2012).
32. A. Andryieuski and A. V. Lavrinenko, "Graphene metamaterials based tunable terahertz absorber: effective surface conductivity approach," Opt. Express **21**(7), 9144–9155 (2013).
33. S. Ke, B. Wang, H. Huang, H. Long, K. Wang, and P. Lu, "Plasmonic absorption enhancement in periodic cross-shaped graphene arrays," Opt. Express **23**(7), 8888–8900 (2015).
34. Y. Fan, B. Wang, K. Wang, H. Long, and P. Lu, "Talbot effect in weakly coupled monolayer graphene sheet arrays," Opt. Lett. **39**(12), 3371–3373 (2014).
35. K. V. Sreekanth, S. Zeng, J. Shang, K. T. Yong, and T. Yu, "Excitation of surface electromagnetic waves in a graphene-based Bragg grating," Sci. Rep. **2**, 737 (2012).
36. V. Gericke, P. Hertel, E. Krätzig, J. P. Nisius, and R. Sommerfeldt, "Light-induced refractive index changes in $LiNbO_3$: Ti waveguides," Appl. Phys. B **44**(3), 155–162 (1987).

## 1. Introduction

Rabi oscillations usually refer to periodic state transitions between two atomic energy levels driven by an electromagnetic wave with the frequency tuned to the energy gap, leading to the periodic emission and reabsorption of photons [1,2]. Such phenomena of alternate conversion of states coupled to external periodic perturbations have also been achieved in semiconductors and condensed matter systems [3,4]. In the past decade, optical Rabi oscillations have been demonstrated in multimode waveguides, photonic crystals and waveguide arrays [5–7]. The optical Rabi oscillation, analogous to its initial conception, refers to the alternate conversion between distinct guided modes as the waveguides undergo a longitudinal periodic modulation of permittivity. As for waveguide arrays, the Bloch modes belonging to different bands will convert to each other and experience an alternate energy exchange during propagation. The effect may find applications in optical switches and spatial mode converters [8–10]. Recently, efficient Rabi oscillations of surface plasmon polaritons (SPPs) have been realized in metal-dielectric waveguides within a subwavelength oscillation period [11]. Similar to metals in visible ranges, graphene can support SPPs in terahertz and far infrared regimes. Compared to the SPPs in metal-dielectric waveguides, the SPPs in graphene possess huge mode

#247890 Received 14 Aug 2015; revised 9 Nov 2015; accepted 13 Nov 2015; published 20 Nov 2015

localization, low propagation loss and flexible tunability [12–15]. By taking advantage of the unique properties, the graphene constructed waveguides and arrays could provide a new platform to investigate Rabi oscillations.

In this work, we propose the graphene-pair arrays (GPAs) composed of periodically arranged graphene pairs to realize Rabi oscillations of SPPs. A graphene pair can support the symmetric and antisymmetric SPP modes [16,17]. Consequently, the GPAs allow two kinds of collective Bloch modes belonging to different bands of the dispersion relation, depending on the symmetry of SPP modes in each individual graphene pair. As the permittivity of the dielectric between graphene undergoes a periodic modulation in the propagation direction, the interband transition could occur. When the permittivity modulation carries a proper transverse momentum, indirect interband transition can be stimulated as well. Here we realize efficient Rabi oscillations with a deep subwavelength period of a few hundred nanometers. The period of Rabi oscillations can also be controlled by tuning the incident Bloch momentums, operation wavelength and chemical potential of graphene.

## 2. Bloch modes in GPAs

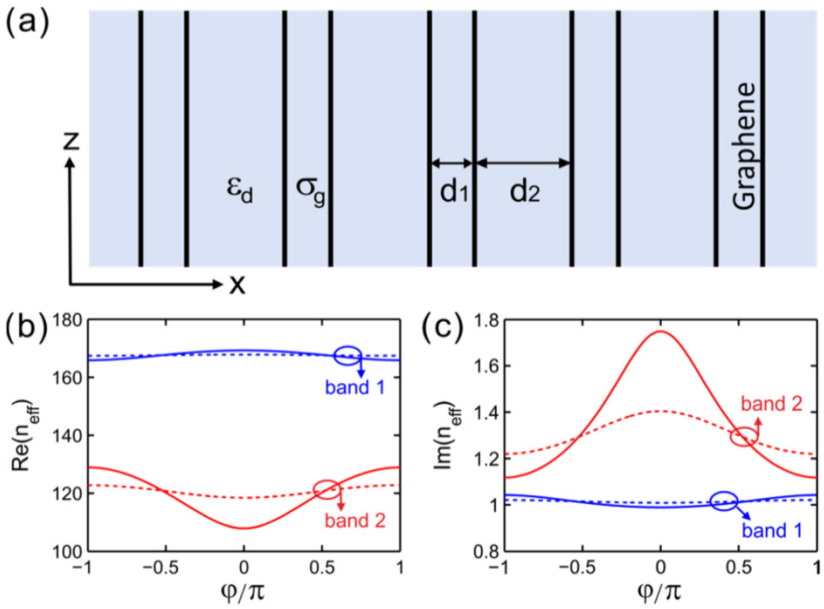


Fig. 1. (a) Schematic of the GPAs. (b) Real part of the effective index ($n_{eff}$) of Bloch modes in the GPAs as a funtion of the Bloch momentum, that is, the band structure of the Bloch modes. Solid and dotted curves denote $d_1$ = 20nm, $d_2$ = 40nm and $d_1$ = 20nm, $d_2$ = 60nm, respectively. (c) Imaginary part of $n_{eff}$ as a function of the Bloch momentum.

We start by investigating the eigen Bloch modes in the GPAs without modulation. As shown in Fig. 1(a), the GPAs are composed of periodically arranged graphene pairs separated by dielectrics. The period of the GPAs is denoted by $d = d_1 + d_2$ with $d_1$ being the spacing of graphene in each pair. The surface conductivity of graphene $\sigma_g(\lambda, \mu_c, \tau, T)$ is modeled by the Kubo formula [18,19], which is determined by the wavelength ($\lambda$), chemical potential of graphene ($\mu_c$), relaxation time ($\tau$), and temperature ($T$). We initially choose $\lambda$ = 10 μm and $\mu_c$ = 0.15 eV. The relaxation time is $\tau$ = 1 ps at room temperature $T$ = 300 K [20]. The relative permittivity of the dielectric medium is assumed as $\varepsilon_d$ = 2.13 [21].

We only consider transverse magnetic (TM) polarized SPPs propagate along $z$ direction. According to Maxwell's equations and the Bloch theorem [22,23], we can obtain the dispersion relation of the Bloch modes

#247890 Received 14 Aug 2015; revised 9 Nov 2015; accepted 13 Nov 2015; published 20 Nov 2015

$$\cos(\varphi) = \cos h(\kappa d) + \xi \sin h(\kappa d) + \frac{\xi^2}{2} \sin h(\kappa d_1) \sin h(\kappa d_2) \qquad (1)$$

where $\kappa = (\beta^2 - \varepsilon_d k_0^2)^{1/2}$, $k_0 = 2\pi/\lambda$, $\beta$ is the propagation constant and $\varphi$ is the Bloch momentum, and $\xi = i\sigma_g \eta_0 \kappa/(\varepsilon_d k_0)$ with $\eta_0$ being the wave impedance in the free space. The effective index of the Bloch modes is given by $n_{\text{eff}} = \beta/k_0$.

Figure 1(b) shows the band structure of the Bloch modes in the GPAs. Note that the band structure here denotes the diffraction relation between the propagation constant or effective index of the Bloch modes and the Bloch momentum [24,25]. There are two bands in the diagram, corresponding to two kinds of Bloch modes in the array. The mode wavelength and propagation distance of the Bloch modes are given by $\lambda_p = \lambda/\text{Re}(n_{\text{eff}})$ and $L_p = [2k_0 \cdot \text{Im}(n_{\text{eff}})]^{-1}$ [26, 27]. As shown in Figs. 1(b) and 1(c), the modes of band 1 have shorter mode wavelengths and longer propagation distances by comparing with the modes of band 2. Particularly for band 1, the modes in the Brillouin zone center have smaller $\lambda_p$ and larger $L_p$ than those at the edges. Concerning band 2, in contrast, the modes at the Brillouin zone edges have shorter mode wavelengths and larger propagation distances. As the period $d$ of the GPAs increases, the coupling of SPPs between adjacent graphene pairs becomes weaker. Consequently, both the real and imaginary parts of the effective indices become flatten (dotted curves), which are more remarkable for band 2.

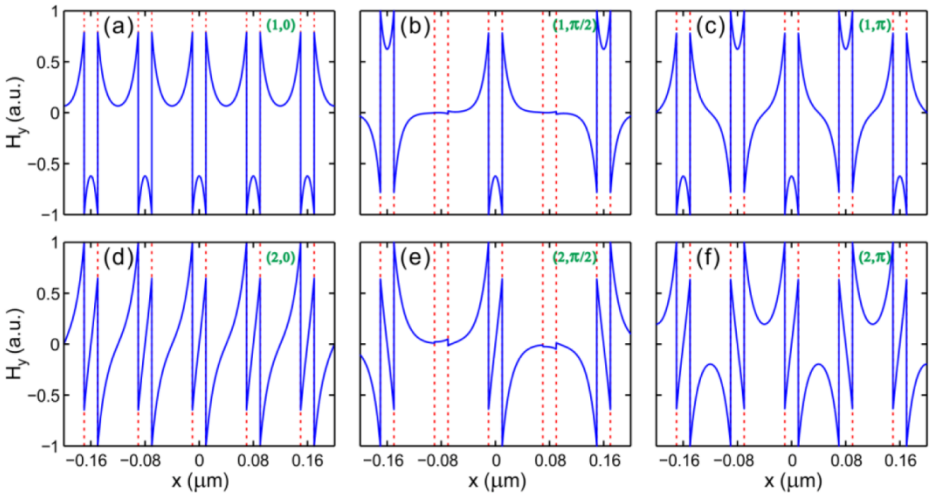


Fig. 2. Normalized transverse magnetic field distributions of the Bloch modes in the GPAs as $d_1$ = 20nm and $d_2$ = 60nm. The positions of graphene sheets are denoted by the red dashed lines. (a)-(c) denote the mode profiles of band 1 as $\varphi$ = 0, $\pi/2$, $\pi$. (d)-(f) Corresponding mode profiles of band 2 as $\varphi$ = 0, $\pi/2$, $\pi$, respectively.

The normalized magnetic field distributions of the Bloch modes are illustrated in Fig. 2. We denote the mode as $\Phi_{m,\varphi}$ with $m$ and $\varphi$ being the band index and Bloch momentum. As each graphene pair can support two kinds of SPP mode, i.e., the symmetric and antisymmetric modes. The Bloch modes of band 1 are formed by the coupling of the symmetric SPP mode in each graphene pair with a phase difference of $\varphi$ between adjacent periods. As shown in Figs. 2(a)-2(c), the mode profiles between adjacent periods are in phase as $\varphi = 0$ and out of phase as $\varphi = \pi$. As $\varphi = \pi/2$, the modes are out of phase in every two periods. The Bloch modes in band 2 are formed by the coupling of antisymmetric SPP mode in each graphene pair. Figures 2(d)-2(f) show the mode profiles in band 2 as $\varphi$ = 0, $\pi/2$ and $\pi$, respectively. The symmetry of the modes in band 2 is opposite to that of the corresponding modes of band 1. The symmetry of the modes is tightly related with the conversion efficiency of Rabi oscillations, which will be discussed in the following.

#247890 Received 14 Aug 2015; revised 9 Nov 2015; accepted 13 Nov 2015; published 20 Nov 2015

### 3. Rabi oscillations of SPP Bloch modes

Now we consider the Rabi oscillations between the Bloch modes in bands 1 and 2 stimulated by the permittivity perturbation. The modulation of permittivity applied to the permittivity dielectrics between graphene is given by

$$\Delta\varepsilon(x,z) = \delta\varepsilon \cdot \Delta\varepsilon(x)\cos(\frac{x\phi}{d})\cos(\frac{2\pi z}{\Lambda_z}) \tag{2}$$

where δε and Δε($x$) are the amplitude and transverse modulation function, ϕ and $\Lambda_z$ are the transverse modulation momentum and the longitudinal modulation period, respectively. The field in the GPAs reads [**E**($x$, $z$), **H**($x$, $z$)] = $\sum_m A_m(z)\exp(i\beta_m z)$[$\mathbf{E}_{m,\varphi}(x)$, $\mathbf{H}_{m,\varphi}(x)$], where $A_m$, $\beta_m$, and [$\mathbf{E}_{m,\varphi}(x)$, $\mathbf{H}_{m,\varphi}(x)$] ($m$ = 1, 2) are the amplitudes, propagation constants, and normalized transverse profiles of the Bloch modes, respectively. By substituting the field distribution into Maxwell's equations and using slow varying amplitude approximation, we can obtain the coupled mode equations [28]

$$\begin{cases} i\dfrac{dA_1}{dz} + \dfrac{M_{21}}{2}A_2\exp[i(\Delta\beta_{21} + \dfrac{2\pi}{\Lambda_z})z] = 0 \\ i\dfrac{dA_2}{dz} + \dfrac{M_{12}}{2}A_1\exp[i(\Delta\beta_{12} - \dfrac{2\pi}{\Lambda_z})z] = 0 \end{cases} \tag{3}$$

where $\Delta\beta_{12} = -\Delta\beta_{21} = \beta_1 - \beta_2$ is the phase mismatch between the two Bloch modes. The coupling coefficient $M_{12}$ is given by [29,30]

$$M_{12} = \frac{\omega\varepsilon_0\int_{-d/2}^{d/2}\delta\varepsilon\cdot\Delta\varepsilon(x)\cos(\frac{x\phi}{d})(E_{1,x}E_{2,x}^* + E_{1,z}E_{2,z}^*)dx}{\sqrt{\int_{-d/2}^{d/2}(2E_{1,x}H_{1,y}^*)dx\int_{-d/2}^{d/2}(2E_{2,x}H_{2,y}^*)dx}} \tag{4}$$

and we have $M_{12} = M_{21}^*$. Under the phase-matching condition $\Delta\beta_{12} = 2\pi/\Lambda_z$, a complete transition between the two Bloch modes will occur. Here we consider the mode of band 1 with Bloch momentum $\varphi_1$ and amplitude $A_1(0)$ is injected into the GPAs and $A_2(0) = 0$ at $z$ = 0. Thus we have $A_1(z) = A_1(0)\cos(|M_{12}/2|z)$ and $A_2(z) = -i(M_{12}/2)^*/|M_{12}/2|\cdot A_1(0)\sin(|M_{12}/2|z)$. The period of Rabi oscillations denoting the length for complete transition is given by $L_c = \pi/|M_{12}|$ [28]. As the transverse modulation momentum is ϕ = 0, only direct interband transition between the modes with $\varphi_2 = \varphi_1$ will take place. While for nonzero modulation momentum (ϕ ≠ 0), indirect interband transition between the Bloch modes with $\varphi_2 - \varphi_1 = \phi$ can be stimulated.

Figure 3 illustrates the coupling coefficient $|M_{12}|$ versus the incident Bloch momentum $\varphi_1$ and momentum difference $\Delta\varphi = \varphi_2 - \varphi_1$. The incident Bloch momentum can be introduced by controlling the phase difference of SPPs in adjacent graphene pairs [23]. The momentum difference between the modes of different bands is generated by the transverse modulation momentum by choosing $\phi = \Delta\varphi$ [7]. In Fig. 3(a), the transverse modulation is odd and reads $\Delta\varepsilon(x) = \sin(2\pi x/d)$. In respect of the direct interband transition as $\Delta\varphi = 0$, $M_{12}$ has the largest modulus at the Brillouin zone center $\varphi_1 = 0$ and decreases from the center to the edges $\varphi_1 = \pm\pi$. While for indirect interband transition $\Delta\varphi = \pi$, the maximum of the coupling coefficient locates at the Brillouin zone edges. In Fig. 3(b), the transverse modulation is even and reads $\Delta\varepsilon(x) = \cos(2\pi x/d)$, the coupling coefficients for both direct ($\Delta\varphi = 0$) and indirect ($\Delta\varphi = \pi$) interband transitions reach their maxima near $\varphi_1 = \pm\pi/2$. As $\varphi_1 = 0$ and $\pm\pi$, the coupling coefficient $|M_{12}| = 0$, leading to the forbiddance of Rabi oscillations. Since the modes possess opposite symmetries for $\varphi_1 = 0$ and $\pm\pi$ as shown in Fig. 2, the overlap integration of $M_{12}$ in Eq. (4) will vanish under an even transverse modulation, and Rabi oscillations are forbidden.

#247890 Received 14 Aug 2015; revised 9 Nov 2015; accepted 13 Nov 2015; published 20 Nov 2015

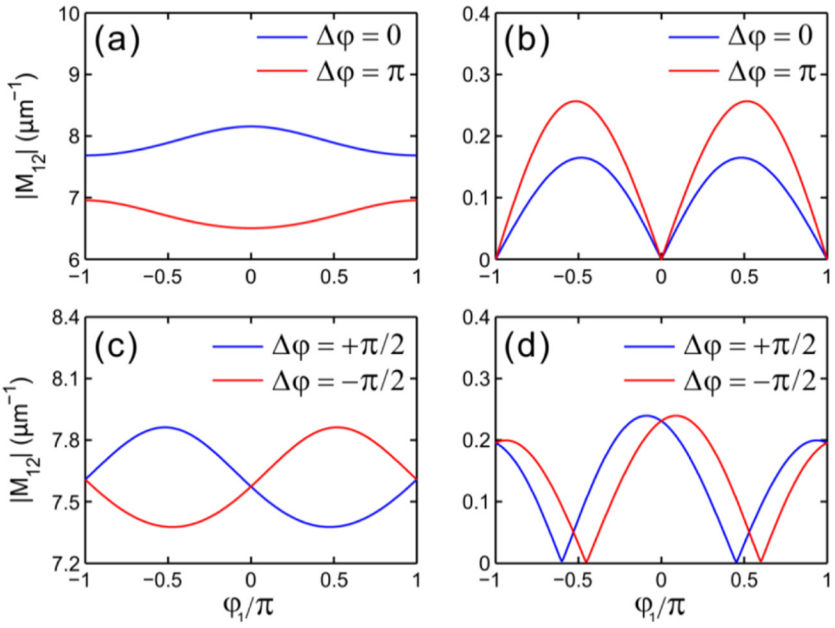


Fig. 3. The coupling coefficient $|M_{12}|$ as a function of incident Bloch momentum $\varphi_1$ and momentum difference $\Delta\varphi = \varphi_2 - \varphi_1$. The modulation amplitude is $\delta\varepsilon = 0.3$ as $d_1 = 20$nm and $d_2 = 60$nm. In (a) and (b) $\Delta\varphi = 0, \pm\pi$ while in (c) and (d) $\Delta\varphi = \pm\pi/2$. In (a) and (c), the transverse modulation is $\Delta\varepsilon(x) = \sin(2\pi x/d)$. In (b) and (d), the transverse modulation is $\Delta\varepsilon(x) = \cos(2\pi x/d)$.

For other incident Bloch momentum $0 < |\varphi_1| < \pi$, due to the broken of mode symmetry, the coupling coefficient $|M_{12}|$ is nonzero. Thus Rabi oscillations can be yielded under both odd and even transverse modulations. Figures 3(c) and 3(d) show the coupling coefficients as the transverse modulation is odd for $\Delta\varepsilon(x) = \sin(2\pi x/d)$ and even for $\cos(2\pi x/d)$. Both situations for $\Delta\varphi = \pm\pi/2$ are considered. Note that $|M_{12}|$ is larger under the odd modulation than the even by more than one order of magnitude. The odd transverse modulation is preferred over the even to reduce the period of Rabi oscillations. As $\Delta\varphi = \pi/2$ shown in Fig. 3(c), $|M_{12}|$ is largest near $\varphi_1 = -\pi/2$ and smallest near $\varphi_1 = \pi/2$. While in Fig. 3(d), the coupling coefficient is largest near $\varphi_1 = 0$ and approaches zero near $\varphi_1 = \pm\pi/2$. Thus by introducing certain transverse modulations, the Rabi oscillations can be controlled arbitrarily.

To validate the theoretical analysis, we also perform numerical simulations by using COMSOL Multiphysics. The results are shown in Fig. 4. In the calculation, graphene is modeled as the surface current boundary condition [31–33]. Figures 4(a) and 4(b) illustrate the analytical and numerical field evolution of the direct interband transition between the Bloch modes $\Phi_{1,0}$ and $\Phi_{2,0}$ under the odd modulation of $\Delta\varepsilon(x) = \sin(2\pi x/d)$. They agree fairly with each other. The analytical and numerical periods of Rabi oscillations (denoted by the horizontal dotted lines) are 0.385 μm and 0.380 μm, respectively. In Fig. 4(c), the mode $\Phi_{1,0}$ is injected from the end of the GPAs under the even modulation of $\Delta\varepsilon(x) = \cos(2\pi x/d)$. It shows that Rabi oscillations do not occur under even modulation for $\varphi_1 = 0$, which confirms the analysis in Fig. 3(b). Figures 4(d) and 4(e) show the field evolution of the indirect interband transitions of $\Phi_{1,0} \leftrightarrow \Phi_{2,\pi}$ and $\Phi_{1,\pi} \leftrightarrow \Phi_{2,0}$ under the odd modulation of $\Delta\varepsilon(x) = \sin(2\pi x/d)$. The periods of Rabi oscillations are 0.48 μm and 0.45 μm, which are larger than those of direct interband transitions shown in Fig. 4(b). It should be mentioned that the propagation loss of SPPs might hinder the observation of Rabi oscillations. In order to implement complete mode conversions, one can reduce the period of Rabi oscillations to combat with negative influence of the propagation loss.

#247890 Received 14 Aug 2015; revised 9 Nov 2015; accepted 13 Nov 2015; published 20 Nov 2015

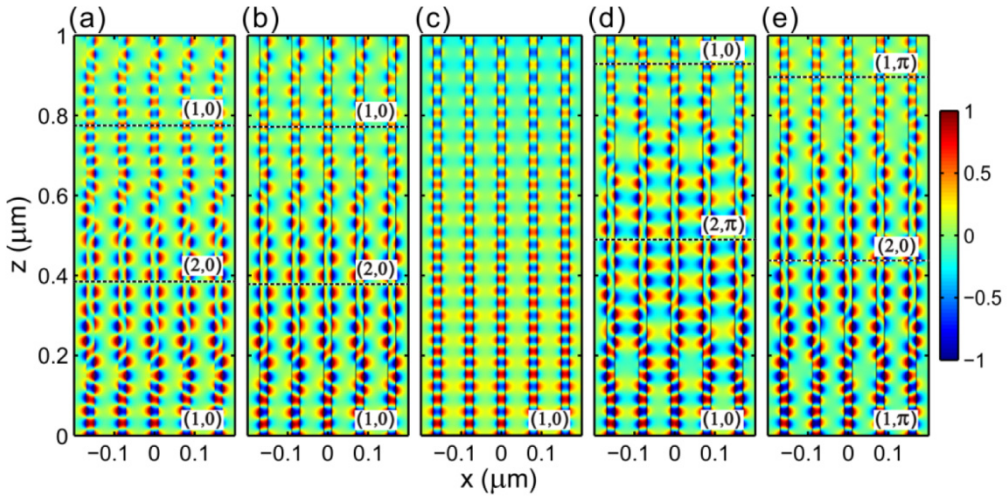


Fig. 4. Analytical and simulated magnetic field ($H_y$) evolution of Rabi oscillations between the Bloch modes as $d_1$ = 20nm, $d_2$ = 60nm, and δε = 0.3. Black dotted lines denote the positions where complete transitions occur. (a) and (b) Analytical and simulated direct interband transtions of $\Phi_{1,0} \leftrightarrow \Phi_{2,0}$ as $\Delta\varepsilon(x) = \sin(2\pi x/d)$. (c) Bloch mode $\Phi_{1,0}$ as $\Delta\varepsilon(x) = \cos(2\pi x/d)$. (d) and (e) Numerical indirect transitions of $\Phi_{1,0} \leftrightarrow \Phi_{2,\pi}$ and $\Phi_{1,\pi} \leftrightarrow \Phi_{2,0}$ as $\Delta\varepsilon(x) = \sin(2\pi x/d)$.

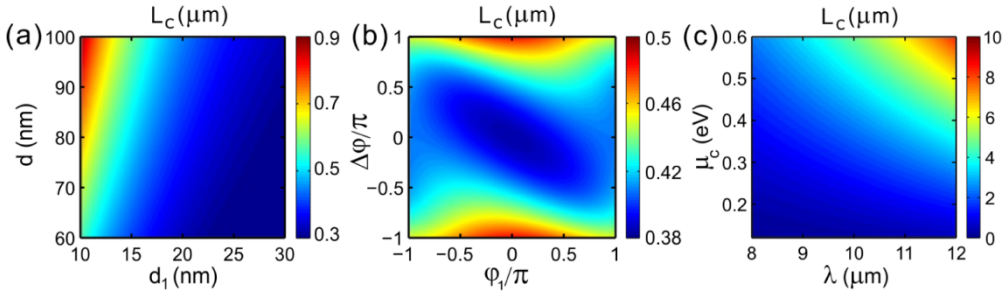


Fig. 5. The period of Rabi oscillations $L_c$ versus different parameters. (a) $L_c$ as a function of $d_1$ and $d$ as $\varphi_1 = 0$ and $\Delta\varphi = 0$. (b) $L_c$ as a function of $\varphi_1$ and $\Delta\varphi$ as $d_1$ = 20nm and $d$ = 80 nm. In (a) and (b) λ = 10 μm and $\mu_c$ = 0.15 eV. (c) The influence of λ and $\mu_c$ on the period of Rabi oscillations for $\varphi_1 = \pi$ and $\Delta\varphi = 0$ as $d_1$ = 20nm and $d$ = 80 nm.

Figure 5 illustrates the influence of other parameters on the period of Rabi oscillations as δε = 0.3 and $\Delta\varepsilon(x) = \sin(2\pi x/d)$. In Fig. 5(a), the oscillation period as a function of the spacing of each graphene pair and the period of the GPAs is investigated. As $d_1$ is fixed, the period of Rabi oscillations increases as $d$ increases. The coupling of SPPs between adjacent graphene pairs becomes weaker as $d$ increases, making the oscillation period increase. For fixed $d$, the period of Rabi oscillations decreases as $d_1$ increases. It shows that the GPAs with close $d_1$ and $d_2$ can benefit the occurrence of Rabi oscillations. In Fig. 5(b), we investigate the influence of incident Bloch momentum and momentum difference on the period of Rabi oscillations as $d_1$ = 20 nm and $d$ = 80 nm. Due to the symmetry of the band structure, the diagram is central symmetric, that is, $L_c(\varphi_1, \Delta\varphi) = L_c(-\varphi_1, -\Delta\varphi)$. As $\varphi_1$ is fixed, $L_c$ increases as $\Delta\varphi$ increases. The oscillation period is smallest for direct transition as $\varphi_1 = 0$, $\Delta\varphi = 0$ and largest for indirect transition as $\varphi_1 = 0$, $\Delta\varphi = \pm\pi$. Figure 5(c) illustrates the influence of incident wavelength and chemical potential of graphene on the period of Rabi oscillations. The oscillation period increases as λ or $\mu_c$ increases. In terahertz range, the intraband transition of electrons in graphene dominates, leading to a Drude-like surface conductivity of $\sigma_g = ie^2\mu_c/[\pi\hbar^2(\omega + i\tau^{-1})]$ [34]. The transverse decay constant of SPPs in a single-layer graphene is $\kappa_{sp} = 2i\varepsilon_d k_0/(\sigma_g\eta_0)$

#247890 Received 14 Aug 2015; revised 9 Nov 2015; accepted 13 Nov 2015; published 20 Nov 2015

[16], thus we have $\mathrm{Re}(\kappa_{sp}) = 8c\varepsilon_d\hbar^2\pi^3/(\eta_0\mu_c\lambda^2e^2)$ with $c$, $e$, $\hbar$ being the speed of light in vacuum, the electron charge and reduced Planck constant, respectively. $\mathrm{Re}(\kappa_{sp})$ decreases as $\lambda$ or $\mu_c$ increases, making the SPP mode more weakly confined to the surface of graphene. Consuquently, the contribution of the mode products in a period to the overlap integration of $M_{12}$ in Eq. (4) becomes less, resulting in the increase of oscillation period.

In terms of the experimental implementions, the graphene-pair arrays can be fabricated as follows [35]. Firstly, a dielectric film with a thickness of nanometers is coated on the substrate by using PLD or CVD method. Then a graphene sheet, usually grown on the cooper foil, can be transferred onto the dielectric film in the $Fe(NO_3)_3$ solution. After the graphene is adhered on the first dielectric film, we can repeat the processes of coating dielectric films and transferring graphene until the desirable layers are achieved. The thickness of dielectric is controllable during the coating process in order to form the pair array structure. The longitudinal permittivity modulation could be realized by holographic recording technique with a two-beam interference setup. As the dielectric material is photorefractive, the required variation of the permittivity can be controlled by the interference intensity which is recorded by the photorefractive dielectrics [7, 36]. On the other hand, the transverse modulation of the permittivity is realizable by coating multiple dielectric layers with distinct permittivity according to the desirable permittivity profile between the graphene sheets.

## 4. Conclusions

In conclusion, we investigate the Rabi oscillations of SPP Bloch modes in GPAs. The modes belonging to different bands are formed by the coupling of symmetric and antisymmetric SPP modes in individual graphene pairs. The interband transitions can be stimulated as the dielectric permittivity undergoes a longitudinal periodic modulation, leading to the occurrence of Rabi oscillations. The Bloch modes will convert to each other alternatively during propagation. As the modulation carries a transverse momentum, Rabi oscillations will occur as well but accompanied with indirect interband transitions. Due to the opposite symmetries of the Bloch modes at the center and edges of the Brillouin zone, Rabi oscillations are forbidden under even transverse modulation. The period of Rabi oscillations can be squeezed into a deep subwavelength scale of a few hundred nanometers. The oscillation period with direct transition is smaller than that with indirect transition. It can be further reduced by introducing proper modulation functions or optimizing the geometry of GPAs. To reduce the influence of propagation loss, we can reduce the oscillation period by choosing shorter operation wavelength and smaller chemical potential of graphene. The study may find applications in optical switches, couplers, and spatial mode converters.

## Acknowledgments

This work is supported by the 973 Program (No. 2014CB921301), the National Natural Science Foundation of China (NSFC) (Nos. 11304108 and 11104095), and the Specialized Research Fund for the Doctoral Program of Higher Education of China (No. 20130142120091).

#247890 Received 14 Aug 2015; revised 9 Nov 2015; accepted 13 Nov 2015; published 20 Nov 2015